The Astrophysical Journal, 888:124 (8pp), 2020 January 10 https://doi.org/10.3847/1538-4357/ab5daf

Stellar Properties of $z \gtrsim 8$ Galaxies in the Reionization Lensing Cluster Survey

Victoria Strait[1], Maruša Bradač[1], Dan Coe[2], Larry Bradley[2], Brett Salmon[2], Brian C. Lemaux[1], Kuang-Han Huang[1], Adi Zitrin[3], Keren Sharon[4], Ana Acebron[3], Felipe Andrade-Santos[5], Roberto J. Avila[2], Brenda L. Frye[6], Austin Hoag[7], Guillaume Mahler[4], Mario Nonino[8], Sara Ogaz[2], Masamune Oguri[9,10,11], Masami Ouchi[11,12], Rachel Paterno-Mahler[13], and Debora Pelliccia[1,14]

[1] Physics Department, University of California, Davis, CA 95616, USA
[2] Space Telescope Science Institute, Baltimore, MD 21218, USA
[3] Department of Physics, Ben-Gurion University, Be'er-Sheva 84105, Israel
[4] Department of Astronomy, University of Michigan, 1085 South University Avenue, Ann Arbor, MI 48109, USA
[5] Harvard-Smithsonian Center for Astrophysics, 60 Garden Street, Cambridge, MA 02138, USA
[6] Department of Astronomy, Steward Observatory, University of Arizona, 933 North Cherry Avenue, Tucson, AZ 85721, USA
[7] Department of Physics and Astronomy, University of California, Los Angeles, CA 90095-1547, USA
[8] INAF—Osservatorio Astronomico di Trieste, via G.B. Tiepolo 11, I-34131 Trieste, Italy
[9] Research Center for the Early Universe, University of Tokyo, 7-3-1 Hongo, Bunkyo-ku, Tokyo 113-0033, Japan
[10] Department of Physics, The University of Tokyo, 7-3-1 Hongo, Bunkyo-ku, Tokyo 113-0033, Japan
[11] Kavli Institute for the Physics and Mathematics of the Universe (Kavli IPMU, WPI), University of Tokyo, Kashiwa, Chiba 277-8583, Japan
[12] Institute for Cosmic Ray Research, The University of Tokyo, 5-1-5 Kashiwanoha, Kashiwa, Chiba 277-8582, Japan
[13] WM Keck Science Center, 925 North Mills Avenue, Claremont, CA 91711, USA
[14] Department of Physics and Astronomy, University of California, Riverside, CA 92521, USA
Received 2019 May 22; revised 2019 November 16; accepted 2019 November 28; published 2020 January 16

Abstract

Measurements of stellar properties of galaxies when the universe was less than one billion years old yield some of the only observational constraints on the onset of star formation. We present here the inclusion of *Spitzer*/IRAC imaging in the fitting of the spectral energy distribution of the seven highest-redshift galaxy candidates selected from the *Hubble Space Telescope* (*HST*) imaging of the Reionization Lensing Cluster Survey. We find that for six out of eight *HST*-selected $z \sim 8$ sources, the $z \sim 8$ solutions are still strongly preferred over $z \sim 1$–2 solutions after the inclusion of *Spitzer* fluxes, and two prefer a $z \sim 7$ solution, which we defer to a later analysis. We find a wide range of intrinsic stellar masses (5×10^6–$4 \times 10^9\,M_\odot$), star formation rates (0.2–14 $M_\odot\,\mathrm{yr}^{-1}$), and ages (30–600 Myr) among our sample. Of particular interest is A1763-1434, which shows evidence of an evolved stellar population (∼500 Myr) at $z \sim 8$, implying that its first generation of star formation occurred <100 Myr after the Big Bang. SPT0615-JD, a spatially resolved $z \sim 10$ candidate, remains at its high redshift, supported by deep *Spitzer*/IRAC data, and also shows some evidence for an evolved stellar population. Even with the lensed, bright apparent magnitudes of these $z \gtrsim 8$ candidates ($H = 26.1$–27.8 AB mag), only the *James Webb Space Telescope* will be able to exclude the possibility of abnormally strong nebular emission, large dust content, or some combination thereof, and confirm the presence of evolved stellar populations early in the universe.

Unified Astronomy Thesaurus concepts: High-redshift galaxies (734); Broad band photometry (184)

1. Introduction

High-z galaxies are key sources in the epoch of reionization, and to understand the contributions of the $z \sim 8-10$ population by way of ionizing photon production, we need measurements of star formation rate (SFR) and stellar mass. However, in practice, robust constraints on physical properties of $z \sim 8-10$ galaxies are difficult to place. Surveys using lensing and blank fields to target high-z galaxies in recent years have rapidly grown the sample (for a review of theoretical models compared to most observations to date, see Dayal & Ferrara 2018). In particular, measurements of ages of galaxies in the high-z universe have provided one of the few observational probes of the onset of star formation (e.g., Egami et al. 2005; Richard et al. 2011; Huang et al. 2016). The most recent spectroscopically confirmed example by Hashimoto et al. (2018) (see also Zheng et al. 2012; Bradač et al. 2014; Hoag et al. 2018) implies first star formation at ∼250 Myr after the Big Bang, as evidenced by an old stellar population in the galaxy MACS1149-JD.

There are also a number of galaxies that are not yet spectroscopically confirmed and show signs of a possible evolved stellar population at high z. At $z \sim 8$, results for spectral energy distribution (SED) are heavily influenced by near-IR fluxes, since the Balmer/$D_n(4000)$ break (hereafter Balmer break) falls into *Spitzer* channel 1 (3.6 μm, [3.6] or ch1 hereafter) from $z \sim 7$ to 10, requiring *Spitzer* fluxes for robust measurements of stellar mass, SFR, and age. Complicating the problem, strengths of nebular emission lines and dust content at these redshifts are unknown, creating a degeneracy between emission lines and the Balmer break that is difficult to disentangle with the currently available near-IR broadband observations. When a spectroscopic redshift is available, it is sometimes possible to disentangle the degeneracy if the emission lines fall outside a broad band, as in Hashimoto et al. (2018). While the *James Webb Space Telescope* (*JWST*) will ultimately be able to break most of these degeneracies, identifying candidates with broadband photometry for follow-up and an initial investigation of their stellar properties are important scientific goals.

So far, there have been 100–200 $z \gtrsim 8$ candidates identified in *Hubble Space Telescope* (*HST*) surveys that utilize gravitational lensing by massive galaxy clusters and in blank field surveys (e.g., Bradley et al. 2014; Bouwens et al.

2015, 2019; Finkelstein et al. 2015; Oesch et al. 2015; Ishigaki et al. 2018; Morishita et al. 2018; De Barros et al. 2019). Photometric redshifts of this sample are largely based on rest-frame UV + optical photometry (*HST* + *Spitzer*/IRAC), and only a small subset are spectroscopically confirmed. Without a spectroscopic confirmation, *Spitzer* fluxes can aid in removing low-redshift interlopers from these samples. Even with a spectroscopic confirmation, *Spitzer*/IRAC (rest-frame optical) fluxes are essential for robust measurements of stellar properties (González et al. 2011; Ryan et al. 2014; Salmon et al. 2015).

Here we use *HST* and *Spitzer*/IRAC imaging data from the Reionization Lensing Cluster Survey (RELICS, PI Coe) and companion survey *Spitzer*-RELICS (S-RELICS, PI Bradač) to probe rest-frame optical wavelengths of seven $z \gtrsim 8$ candidates originally selected with *HST*. Details of the *HST*-selected high-z candidates can be found in Salmon et al. (2017, 2018, hereafter S17, S18). We present measurements of stellar mass, SFR, and age inferred from *HST* and *Spitzer* broadband fluxes.

In Section 2 we describe *HST* and *Spitzer* imaging data and photometry. In Section 3 we discuss the lens models used in our analysis. In Section 4 we describe our photometric redshift procedure, SED modeling procedure, and calculation of stellar properties. We present the results of our SED fitting and stellar properties in Section 5 and we conclude in Section 6. Throughout the paper, we give magnitudes in the AB system (Oke 1974), and we assume a ΛCDM cosmology with $h = 0.7$, $\Omega_m = 0.3$, and $\Omega_\Lambda = 0.7$.

2. Observations and Photometry

HST reduced images and catalogs are publicly available on the Mikulski Archive for Space Telescopes (MAST[15]) and *Spitzer* reduced images on NASA/IPAC Infrared Science Archive (IRSA[16]). Details of the survey can be found in Coe et al. (2019). Here we focus on the six clusters with $z \gtrsim 8$ candidates (A1763, MACSJ0553-33, PLCKG287+32, AS295, RXC0911+17, and SPT0615-57, Figure 1).

2.1. HST

Each cluster was observed with two orbits of WFC3/IR imaging in F105W, F125W, F140W, and F160W and with three orbits in ACS (F435W, F606W, F814W), with the exception of A1763, which received seven additional WFC3/IR orbits. In this work, we use the catalogs based on a detection image comprising the $0\farcs06$/pixel weighted stack of all WFC3/IR imaging, optimized for detecting small high-z galaxies, described in Coe et al. (2019).

2.2. Spitzer *Data and Photometry*

Each cluster was observed with *Spitzer*/IRAC by a combination of RELICS programs (PI Soifer, #12123, PI Bradač #12005, 13165, 13210) and archival programs. PLCKG287+32, A1763, and SPT0615-57 were observed for 30 hr each in [3.5] and [4.6] channels, including archival data (PI Brodwin #80012). AS295 was observed for 5 hr in each channel, including archival data (PI Menanteau #70149). MACSJ0553-33 was observed for 5.2 hr in each channel including archival data (PI Egami #90218). RXC0911+17 was observed for 5 hr with archival data only (PI Egami #60032). In addition to *Spitzer* and *HST* fluxes, we include *Ks* imaging from VLT-HAWK-I (#0102.A-0619, PI Nonino) for PLCKG287+32 (other clusters do not have such data at present). Reduction details for the *Ks* imaging will be detailed in M. Nonino et al. (2020 in preparation).

Spitzer data reduction and flux extraction is similar to that of the *Spitzer* Ultra-Faint Survey Program (Huang et al. 2016). Full details, including treatment of the intracluster medium, will be described in detail in an upcoming catalog paper (V. Strait et al. 2020 in preparation). Due to the broad point-spread function (PSF) and low resolution ($0\farcs6$/pixel) of *Spitzer* images, we extract fluxes using T-PHOT (Merlin et al. 2015), designed to perform PSF-matched, prior-based, multi-wavelength photometry as described in Merlin et al. (2015, 2016). We do this by convolving a high-resolution image (in this case, F160W) using a low-resolution PSF transformation kernel that matches the F160W resolution to the IRAC (low-resolution) image and fitting a template to each source detected in F160W to best match the pixel values in the IRAC image.

We assess the trustworthiness of the output fluxes using diagnostic outputs $R_{3.6}$ and $R_{4.5}$ (see Table 1), defined as the ratio between the maximum value in the covariance matrix for a given source (i.e., the covariance with the object's closest or brightest source) and the source's own flux variance. Covariance indices $R_{3.6}$ and $R_{4.5}$ are indicators of whether a source is experiencing confusion with a nearby source. In the case of severe confusion and a high covariance index ($R_{3.6}$, $R_{4.5} > 1$), we perform a series of tests involving the input of simulated sources of varying brightnesses to test the confusion limit of that pair of sources. The only source with $R_{3.6}$, $R_{4.5} > 1$ in our sample is SPT0615-JD, and as described in S18, we find that simulated magnitudes brighter than ∼25 can be safely recovered, and sources fainter than that have an additional 0.5 magnitude uncertainty. After testing the inclusion of this additional uncertainty, we conclude that the upper 1σ bounds of SPT0615-JD are trustworthy as lower limits in magnitude (i.e., the flux of the source could be fainter than the extracted fluxes but not brighter).

2.3. Sample Selection

The selection criteria for all high-redshift ($z_{\rm peak} \geqslant 5.5$) *HST*-selected RELICS objects are described in S17 ($z \sim 6-8$ candidates) and S18 ($z \sim 10$ candidate SPT0615-JD). This paper focuses on $z \sim 8$ candidates from the S17 sample and the $z \sim 10$ candidate from S18 that still have $z_{\rm peak} \geqslant 7.5$ when *Spitzer* fluxes are included in their photometry. We find that the $z \sim 10$ candidate from S18 and six of the eight $z \sim 8$ candidates in S17 remain likely to be at $z \geqslant 7.5$ upon inclusion of *Spitzer* fluxes (Table 1). The other two $z \sim 8$ candidates from S17 (SPT0615-57-1048 and PLCKG287+32-2013) were moved into the $z \sim 7$ bin. We will explore these candidates in a future work.

3. Lens Models

In order to correct for magnification from lensing, relevant for SFRs and stellar masses, we use lens models created by the RELICS team. We use three lens modeling codes to produce the models for the clusters described here: `Lenstool` (Jullo & Kneib 2009) for MACSJ0553-33 and SPT0615-57, Glafic (Oguri 2010) for RXC0911+17, and a light-traces-mass (LTM)

[15] https://archive.stsci.edu/prepds/relics/
[16] https://irsa.ipac.caltech.edu/data/SPITZER/SRELICS/

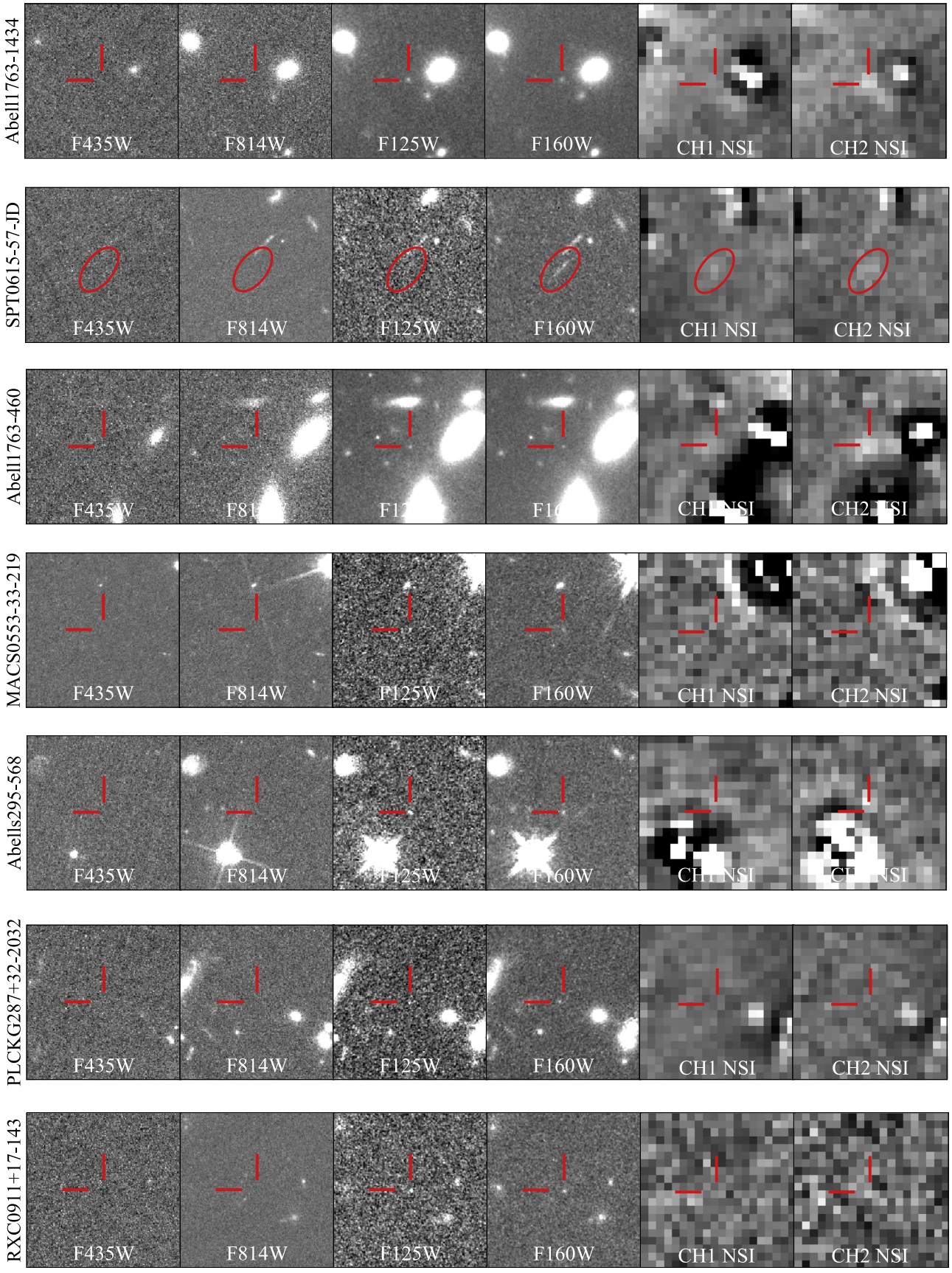

Figure 1. Image stamps for each candidate, $12'' \times 12''$, of two ACS bands (F435W and F814W), two WFC3 bands (F125W and F160W), *Spitzer*/IRAC Ch1 ([3.6]) and Ch2 ([4.5]). The *Spitzer* cutouts are neighbor-subtracted images (NSI), i.e., everything in the field is subtracted except the high-z source. Red lines mark the location of the source.

Table 1
$z \gtrsim 8$ Galaxy Candidates and Selected Photometry

Object ID	R.A. (deg.)	Decl. (deg.)	F160W[a] (mag)	*Ks* (mag)	[3.6][b] (mag)	$R_{3.6}$[c]	[4.5][b] (mag)	$R_{4.5}$[c]
A1763-1434	203.8333744	+40.9901793	26.1 ± 0.1		25.5 ± 0.4	0.29	24.5 ± 0.2	0.28
A1763-0460	203.8249758	+41.0091170	27.8 ± 0.2		>25.9	0.37	24.5 ± 0.2	0.39
MACSJ0553-33-0219	88.3540349	−33.6979484	27.2 ± 0.2		25.0 ± 0.3	0.34	25.5 ± 0.6	0.34
PLCKG287+32-2032	177.7225936	−28.0850703	26.7 ± 0.2	26.6 ± 0.3	>26.6	0.53	>26.4	0.59
SPT0615-JD	93.9792550	−57.7721477	25.8 ± 0.1		26.0 ± 0.6	1.43	25.4 ± 0.4	1.13
RXC0911+17-0143	137.7939712	+17.7897516	26.5 ± 0.1		>26.4	0.05	>26.1	0.04
AS295-0568	41.4010242	−53.0405184	26.3 ± 0.1		>26.2	0.16	>26.3	0.14

Notes.
[a] Total lensed magnitude (`FLUX_ISO`).
[b] *Spitzer*/IRAC channels 1 and 2 magnitudes measured with the same aperture as *HST* magnitudes and 1σ error. If detection is $< 1\sigma$, 1σ lower limit is reported.
[c] Covariance index for *Spitzer*/IRAC channels (Section 2.2).

Table 2
Results of Photometric Redshift and Stellar Population Modeling

Object ID	z_{peak}[a]	μ_{med}[b]	$M_{stellar}$[c] ($10^9\ M_\odot$)	SFR[c] ($M_\odot\ yr^{-1}$)	Age[d] (Myr)	sSFR[e] (Gyr^{-1})	$E(B-V)$[f] (mag)	M_{1600}[g] (mag)
A1763-0460[h]	$8.9^{+0.2}_{-0.8}$	$2.9^{+0.9}_{-1.0}$	$0.3^{+4.3}_{-0.2}(^{+0.2}_{-0.1})$	$1.2^{+10.4}_{-0.6}(^{+0.6}_{-0.3})$	510^{+60}_{-500}	$2.9^{+102.1}_{-0.3}$	$0.00^{+0.25}_{-0.00}$	$-18.4^{+0.3}_{-0.2}(^{+0.3}_{-0.5})$
A1763-1434	$8.2^{+0.6}_{-0.2}$	$2.0^{+0.5}_{-0.4}$	$4.3^{+2.4}_{-2.1}(^{+1.1}_{-0.7})$	$13.7^{+9.1}_{-4.0}(^{+3.4}_{-2.3})$	510^{+60}_{-190}	$2.9^{+1.5}_{-0.3}$	$0.10\pm^{0.05}_{0.00}$	$-20.2^{+0.2}_{-0.3}(^{+0.2}_{-0.2})$
AS295-0568[h]	$8.1^{+0.3}_{-0.7}$	$4.0^{+1.5}_{-0.4}$	$0.07^{+0.03}_{-0.02}(^{+0.01}_{-0.01})$	$2.4^{+2.2}_{-0.4}(^{+0.3}_{-0.7})$	28^{+13}_{-16}	$41.2^{+47.3}_{-11.9}$	$0.00^{+0.50}_{-0.00}$	$-19.4^{+0.2}_{-0.1}(^{+0.3}_{-0.1})$
MACSJ0553-33-0219	$8.2^{+0.2}_{-2.4}$	$6.5^{+0.7}_{-0.6}$	$0.6^{+0.9}_{-0.5}(^{+0.1}_{-0.1})$	$1.8^{+2.5}_{-1.3}(^{+0.2}_{-0.2})$	570^{+240}_{-320}	$2.6^{+2.9}_{-0.7}$	$0.20^{+0.10}_{-0.20}$	$-17.9^{+0.8}_{-0.2}(^{+0.1}_{-0.1})$
PLCKG287+32-2032	$7.9^{+0.5}_{-0.9}$	36^{+12}_{-6}	$0.005^{+0.003}_{-0.002}(^{+0.001}_{-0.001})$	$0.2^{+2.5}_{-0.1}(^{+0.0}_{-0.1})$	31^{+9}_{-11}	$36.9^{+18.4}_{-7.7}$	$0.05^{+0.10}_{-0.05}$	$-16.5^{+0.4}_{-0.3}(^{+0.3}_{-0.2})$
RXC0911+17-0143	$8.1^{+0.4}_{-0.6}$	$1.5^{+0.2}_{-0.2}$	$0.2^{+0.8}_{-0.1}(^{+0.0}_{-0.0})$	$5.6^{+10.6}_{-1.4}(^{+0.9}_{-0.7})$	34^{+200}_{-20}	$33.9^{+71.0}_{-28.0}$	$0.00^{+0.05}_{-0.00}$	$-20.3^{+0.2}_{-0.1}(^{+0.1}_{-0.2})$
SPT0615-JD	$10.2^{+1.1}_{-0.5}$	$6.0^{+2.7}_{-1.7}$	$0.4^{+0.7}_{-0.3}(^{+0.2}_{-0.1})$	$6.2^{+6.9}_{-3.2}(^{+2.5}_{-1.9})$	80^{+320}_{-70}	$15.4^{+73.0}_{-11.9}$	$0.05^{+0.05}_{-0.05}$	$-19.8^{+0.2}_{-0.6}(^{+0.4}_{-0.4})$

Notes.
[a] Peak redshift and 68% confidence level (CL) in PDF described in Section 2.
[b] Median magnification factor found using corresponding lens model. μ_{med} is assumed in calculations of SFR and $M_{stellar}$.
[c] Intrinsic stellar mass and SFR, assuming $\mu = \mu_{med}$. Uncertainties include statistical 68% CLs from photometry and redshift. To use a different magnification value, multiply the quantity by $1/f_\mu$, where $f_\mu \equiv \mu/\mu_{med}$. In parentheses, 68% CLs from magnification only, assuming median $M_{stellar}$ or SFR value.
[d] Time since the onset of star formation assuming a constant SFR.
[e] Specific SFR, sSFR ≡ SFR/$M_{stellar}$.
[f] Dust color excess of stellar emission. SMC dust law assumed.
[g] Rest-frame 1600 Å magnitude assuming μ_{med}, derived from the observed F160W magnitude including a small template-based *k*-correction. Uncertainties include statistical 68% CLs from photometry and redshift. To use a different magnification value, use $M_{1600} - 2.5\log(f_\mu)$. In parentheses, 68% CLs from magnification only, assuming median F160W magnitude and z_{peak}.
[h] Bright neighboring galaxy may cause additional uncertainty in *Spitzer* fluxes.

method (Zitrin et al. 2013) for AS295, PLCKG287+32, and A1763. Full details of the SPT0615-57 `Lenstool` model can be found in Paterno-Mahler et al. (2018), and the LTM models for AS295 and PLCKG287+32 are described in detail by Cibirka et al. (2018) and Zitrin et al. (2017), respectively.

The remaining three clusters will have details available in the future, and all models are available on MAST.[17] Our `Lenstool` model of MACSJ0553-33 uses nine multiply imaged systems as constraints, three of which are spectroscopically confirmed, including arc system 1 of Ebeling et al. (2017), and our Glafic model of RXC0911+17 uses three multiply imaged systems with photometric redshifts as constraints.

We find no clear multiple image constraints in A1763, but are able to make an approximate model for the cluster using the LTM method, which relies on the distribution and brightness of cluster galaxies. One should be cautious in interpreting magnifications in this field, however, because in the case of A1763 where there are no visible constraints, we adopt a range of mass-to-light normalization using typical values from other clusters. Median magnifications for the high-z candidates are listed in Table 2, and treatment of their statistical uncertainties is described in Section 4.3.

[17] https://archive.stsci.edu/prepds/relics/

4. SED Fitting

4.1. Photometric Redshifts and Stellar Properties

To obtain a probability distribution function (PDF) and peak redshift, we use Easy and Accurate Redshifts from Yale (EAzY, Brammer et al. 2008), a redshift estimation code that compares the observed SEDs to a set of stellar population templates. For redshift fitting, we use the base set of seven templates from Bruzual & Charlot (2003, BC03), allowing linear combinations. EAzY performs a χ^2 minimization on a redshift grid, which we define to range from $z = 0.01$ to 12 in linear steps of $\Delta z = 0.01$, and computes a PDF from the minimized χ^2 values, where we assume a flat prior.

To calculate stellar properties of our candidates, we use a set of ∼2000 stellar population synthesis templates, also from BC03, this time not allowing linear combinations. We

assume a Chabrier initial mass function (Chabrier 2003) between 0.1 and 100 $M_{\odot}$, metallicity of 0.02 $Z_{\odot}$, and constant star formation history. We allow age to range from 10 Myr to the age of the universe at the redshift of the source. We assume the Small Magellanic Cloud dust law with $E_{\star}(B-V) = E_{\rm gas}(B-V)$ with step sizes of $\Delta E(B-V) = 0.05$ for $E(B-V) = 0$–0.5 mag and $\Delta E(B-V) = 0.1$ for $E(B-V) = 0.5$–1 mag.

Since it has been shown that nebular emission can contribute significant flux to broadband photometry (e.g., Schaerer & de Barros 2010; Smit et al. 2014), we add nebular emission lines and continuum to the BC03 templates using strengths determined by nebular line ratios in Anders & Fritze-v. Alvensleben (2003) for a metallicity of 0.02 $Z_{\odot}$, where we calculate hydrogen recombination line strength using the relation from Leitherer & Heckman (1995), scaling from integrated Lyman-continuum flux. In addition, we include Lyα, with expected strengths calculated using the ratio of Hα to Lyα photons calculated for Case B recombination (high optical depth, $\tau \sim 10^4$) in Brocklehurst (1971), assuming a Lyα escape fraction of 20%. While this is, perhaps, an overestimate at these redshifts (e.g., Hayes et al. 2010, though see Oesch et al. 2015; Stark et al. 2017), we conservatively adopt this value to allow for a higher contribution from the Lyα line. We describe calculation of statistical uncertainties with a Monte Carlo simulation in Section 4.3.

4.2. Biases and Systematic Uncertainties

Star formation history (SFH) and initial mass function are known to introduce large systematic biases in age and SFR (Lee et al. 2009), although at high z this is alleviated to some degree due to the fact that the universe is only ∼750 Myr old at $z \sim 8$ (Pacifici et al. 2016). Since SFHs of our sources are not known a priori, we made a choice to use a simple constant star-forming model. Importantly, this may not be the most appropriate for high-redshift, star-forming galaxies, so we also run our analysis using a suite of delayed tau models, which include an exponential component, for comparison. We find that there are no significant biases in age, and a 0.5 dex bias toward smaller stellar masses and SFRs when adopting a delayed tau SFH.

There is also a well-known degeneracy between dust, age, and metallicity parameters, so a lack of constraints on dust attenuation can lead to a large uncertainty (∼0.5–1 dex) on SFR and stellar mass (Huang et al. 2016). This is a particularly difficult degeneracy to break for objects at $z \sim 8$ because the SED near the UV slope is not well sampled. We explore a subset of these biases in our own sample, largely finding what is reflected in the literature. We find that changing the assumed dust attenuation law from one with the shape of the SMC or Milky Way extinction law biases stellar masses and SFRs higher by ∼0.5 dex. On the other hand, large changes in the metallicity (0.02 $Z_{\odot}$–$Z_{\odot}$) introduce subdominant systematic errors on SFR, stellar mass, or age ($\lesssim$0.1 dex).

An additional uncertainty is the equivalent width distribution of nebular emission lines at high z, particularly [O III] + Hβ, which falls in *Spitzer*/IRAC [4.5] at $z \sim 8$. Strong emission lines ($\gtrsim$1000 Å) have the potential to boost broadband fluxes, as much or more than a strong Balmer break can boost the flux, potentially biasing stellar mass, sSFR, and age (Labbé et al. 2013). While we do not fully explore the effects of this degeneracy, we do adopt standard assumptions with regard to emission lines (Section 4.1).

4.3. Statistical Uncertainties

To understand the statistical uncertainties from photometry and redshift in the stellar properties, we perform a Monte Carlo (MC) simulation on each object. For each iteration, we sample from the redshift PDF (calculated using EAzY default templates allowing linear combination, as described in Section 4.1) and recompute the photometry for each band by Gaussian sampling from the estimated errors (Table 1). In the case of upper limits, we do not perturb the fluxes. For each of 1000 iterations we use EAzY to find a best-fit template (from the template set for stellar properties described in Section 4.1) for the photometry, fixing the redshift to that which was sampled from the PDF on each iteration. The uncertainties on stellar properties reflect only statistical uncertainties and do not include systematic uncertainties associated with choices in initial mass function, star formation history, metallicity, dust law, or the Balmer break versus emission line degeneracy.

Regarding the effect of magnification uncertainties on our stellar properties, statistical uncertainties often underestimate the true uncertainties in magnification due to differences in model assumptions. Median systematic uncertainties from CLASH clusters are typically ∼20% (Zitrin et al. 2015), although differences may be larger at larger magnifications (Meneghetti et al. 2017). We calculated the differences between models for the only cluster with multiple models available, SPT0615-57, and found that for SPT0615-JD, $\mu_{\rm med}$ ranged from 2.5 to 6.3. We report μ-scalable $M_{\rm stellar}$, SFR, and M_{1600} assuming our median magnification $\mu_{\rm med}$, with uncertainties from magnification on the quantity in parentheses in Table 2. To use a different magnification than is listed, one can multiply the appropriate μ-scalable value by $1/f_{\mu}$, where $f_{\mu} \equiv \mu/\mu_{\rm med}$.

5. Results

The results from SED fitting and MC simulations are listed in Table 2 as the median and 1σ statistical uncertainty on stellar properties for all objects. The redshift PDFs for all sources reflect that the high-redshift solution is preferred significantly more often than the low-redshift solution in each case ($P(z < 7) < 1\%$). We find a wide range of intrinsic stellar masses ($5 \times 10^6\ M_{\odot}$–$4 \times 10^9\ M_{\odot}$), SFRs (0.2–14 $M_{\odot}\ {\rm yr}^{-1}$), and ages (30–600 Myr) among the sample, and highlight, in particular, two objects that show a preference for an evolved stellar population, A1763-1434 and SPT0615-JD.

5.1. A1763-1434

The SED fitting and MC simulation results are shown in Figures 2 and 3. We find that A1763-1434 is a relatively massive galaxy with an evolved stellar population (∼500 Myr). Using the assumptions outlined in Section 4.1, we find a median intrinsic stellar mass of $4.3^{+2.4}_{-2.1} \times 10^9\ M_{\odot}$ and median age of 510^{+60}_{-190} Myr (see Table 2 for uncertainties from μ). The distribution of the time since the Big Bang until the onset of star formation in this galaxy is shown in the rightmost panel of Figure 3, and implies that the oldest stars in this galaxy started forming <100 Myr after the Big Bang. A1763-1434 prefers the oldest possible solution the large majority of the time: 73% of solutions prefer first star formation <100 Myr after the Big Bang, though we cannot exclude the possibility that abnormally

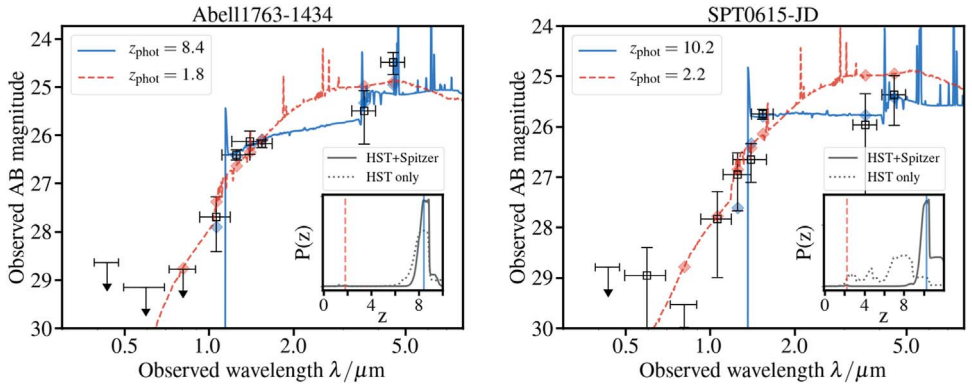

Figure 2. Best-fit SEDs for A1763-1434 and SPT0615-JD, fit to BC03 templates assuming a constant star formation history, 0.02 $Z_{\odot}$ metallicity (m32; Bruzual & Charlot 2003), Lyα escape fraction $f_{esc} = 20\%$, and SMC dust law. Solid blue lines show best-fit templates and dashed red lines show templates best fit at the associated low-redshift peak in $P(z)$. Translucent blue diamonds show expected photometry for best fit and translucent red diamonds show expected photometry for low-redshift fit. The inset shows $P(z)$ calculated from EAzY while allowing for linear combinations of the default base set of BC03 templates. The solid gray line shows probability with *HST* and *Spitzer* fluxes, dotted gray shows probability with *HST* fluxes only. Vertical lines correspond to best-fit and low-redshift best-fit solutions.

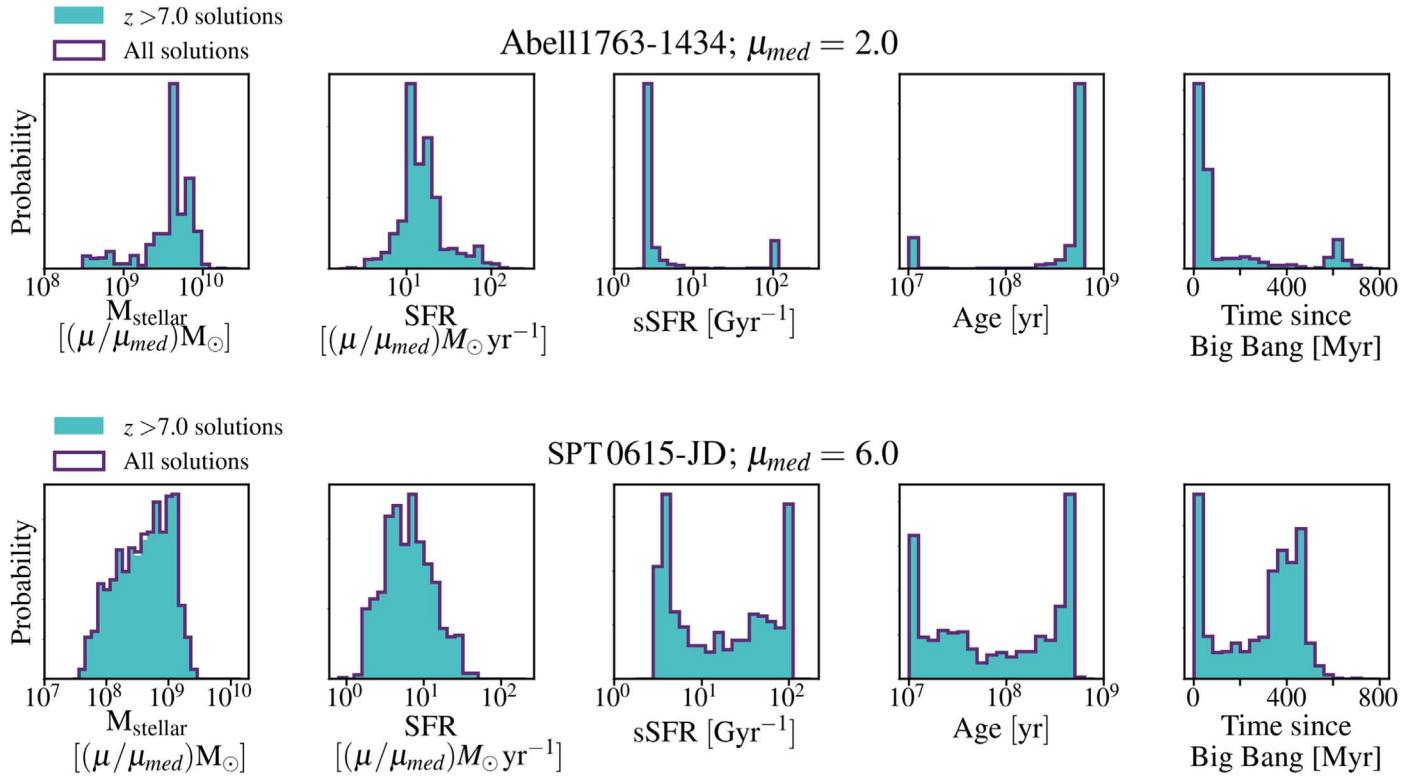

Figure 3. Distributions of stellar properties for A1763-1434 (top) and SPT0615-JD (bottom) explored by Monte Carlo simulation described in Section 4.3. From left to right, each panel shows stellar mass, star formation rate, specific star formation rate (SFR/$M_{stellar}$), age, and time since the Big Bang until the onset of star formation. High-redshift solutions are shown in turquoise and all solutions, including low-redshift ones, are shown in purple outline. There is no significant distinction between the two as the probability for low redshift is small. The redshifts explored by the MC simulation reflect the shapes of respective PDFs for each object in Figure 2.

strong nebular emission, large dust content, or some combination thereof could serve to decrease the estimated age.

We detect this source in *Spitzer*/IRAC [3.6] and [4.5] at 2σ and 5σ, respectively. In [4.5], the detection is significantly discrepant with the predicted photometry ($\sim 2\sigma$) for the high-z solution (blue diamond in Figure 2). This could be indicative of a second, younger stellar population, high levels of dust, strong [O III] emission, or some combination thereof. Assuming the boost in [4.5] is from strong [O III] + Hβ, we increase the rest-frame equivalent width from our best-fit value of $\sim$215 Å to $\sim$1000 Å. This exercise yields a 0.54 magnitude boost in [4.5], roughly the amount needed to match the detection. Thus, even with extreme [O III] + Hβ equivalent widths, we still require a significant Balmer break to fit the photometry well. We are not able to fully break this degeneracy with our current data, but possible improvements include sampling the UV slope with more broad/medium-band filters (e.g., Whitaker et al. 2011) to understand dust content, a spectroscopic redshift to mitigate redshift uncertainty, and a constraint on [O III] equivalent width, perhaps using other emission lines such as C III] (e.g., Maseda et al. 2017; Senchyna et al. 2017). Ultimately, *JWST*

will allow us to measure continuum and emission lines to resolve the degeneracy.

5.2. SPT0615-JD

We find that SPT0615-JD is a typical galaxy with intrinsic stellar mass of $4.4^{+6.8}_{-3.1} \times 10^8 M_\odot$, SFR of $6.2^{+6.9}_{-3.2} M_\odot\ \mathrm{yr}^{-1}$, and a bimodal age distribution preferring either the oldest age solution possible or a younger population with first star formation ∼400 Myr after the Big Bang.

Assuming $z = 10.2$, the IRAC bands are uncontaminated by [O III] + Hβ. The Balmer break, however, still remains fairly unconstrained due to confusion-limited *Spitzer* fluxes. We report a PDF with a small secondary peak, noting an insignificant probability of a low-redshift solution (<1%). This source has two marginal detections (1σ–2σ) in *Spitzer*/IRAC, which we plot in Figure 2 as 1σ lower limits in magnitude. These limits are tighter by 0.2 mag in [3.6] and 0.5 mag in [4.5] compared to fluxes reported in S18, a result of deeper data from our program that became available after the S18 analysis. This increases the probability of a high-z solution and strengthens the argument made in S18 that all low-z solutions require brighter *Spitzer* fluxes than our upper limits allow, and all high-z solutions are well fit with fluxes fainter than the limits.

5.3. Other Sources

For the remaining five sources, we find a range of masses, with the least massive being PLCKG287+32-2032 at an intrinsic stellar mass of $5^{+3}_{-2} \times 10^6\, M_\odot$. We report 1$\sigma$ magnitude limits for non-detections in *Spitzer* for MACSJ0553-33-0219, PLCKG287+32-2032, and RXC0911 +17-143 with the exception of a 3σ detection in [3.6] for MACSJ0553-33-0219 (Table 1).

AS295-0568 and A1763-0460 are both likely contaminated with bright nearby sources, and their resulting stellar properties could be affected by systematic uncertainties not accounted for in error bars, including effects due to subtraction. The redshift solutions for these two sources are robust to variances in *Spitzer* fluxes, and even to excluding the *Spitzer* fluxes entirely.

6. Conclusions

We present SFRs, stellar masses, ages, and sSFRs for seven $z \gtrsim 8$ candidates from RELICS. All candidates have robust high-redshift solutions ($P(z > 7.5) > 0.95$) after the inclusion of *Spitzer*/IRAC [3.6] and [4.5] fluxes and are reasonably bright (⩽27.8 magnitudes). We highlight, in particular, A1763-1434, which shows evidence for an evolved stellar population (∼500 Myr) at a high best-fit redshift of $z = 8.2^{+0.6}_{-0.2}$, implying the onset of star formation <100 Myr after the Big Bang. We also present a follow-up analysis of SPT0615-JD, the highest-redshift candidate from the RELICS sample at $z = 10.2^{+1.1}_{-0.5}$, also showing some evidence for an evolved stellar population. In both cases, a younger stellar population with extreme nebular emission, large dust content, or some combination thereof, could also explain the observed fluxes. While we cannot fully disentangle the degeneracies associated with SED fitting at $z \sim 8$, all candidates presented here have interesting stellar properties that would benefit from further study with *JWST*.

Based on observations made with the NASA/ESA *Hubble Space Telescope*, obtained at the Space Telescope Science Institute, which is operated by the Association of Universities for Research in Astronomy, Inc., under NASA contract NAS 5-26555. Observations were also carried out using *Spitzer Space Telescope*, which is operated by the Jet Propulsion Laboratory, California Institute of Technology under a contract with NASA.

M.B. and V.S. acknowledge support by NASA through ADAP grant 80NSSC18K0945, NASA/*HST* through HST-GO-14096, HST-GO-13666 and two awards issued by *Spitzer*/JPL/Caltech associated with SRELICS_DEEP and SRELICS programs.

ORCID iDs

Victoria Strait https://orcid.org/0000-0002-6338-7295
Maruša Bradač https://orcid.org/0000-0001-5984-0395
Dan Coe https://orcid.org/0000-0001-7410-7669
Larry Bradley https://orcid.org/0000-0002-7908-9284
Brett Salmon https://orcid.org/0000-0002-7453-7279
Kuang-Han Huang https://orcid.org/0000-0001-7826-6448
Adi Zitrin https://orcid.org/0000-0002-0350-4488
Keren Sharon https://orcid.org/0000-0002-7559-0864
Ana Acebron https://orcid.org/0000-0003-3108-9039
Felipe Andrade-Santos https://orcid.org/0000-0002-8144-9285
Austin Hoag https://orcid.org/0000-0001-8989-2567
Guillaume Mahler https://orcid.org/0000-0003-3266-2001
Masamune Oguri https://orcid.org/0000-0003-3484-399X
Masami Ouchi https://orcid.org/0000-0002-1049-6658
Rachel Paterno-Mahler https://orcid.org/0000-0003-3653-3741

References

Anders, P., & Fritze-v. Alvensleben, U. 2003, A&A, 401, 1063
Bouwens, R. J., Illingworth, G. D., Oesch, P. A., et al. 2015, ApJ, 803, 34
Bouwens, R. J., Stefanon, M., Oesch, P. A., et al. 2019, ApJ, 880, 25
Bradač, M., Ryan, R., Casertano, S., et al. 2014, ApJ, 785, 108
Bradley, L. D., Zitrin, A., Coe, D., et al. 2014, ApJ, 792, 76
Brammer, G. B., van Dokkum, P. G., & Coppi, P. 2008, ApJ, 686, 1503
Brocklehurst, M. 1971, MNRAS, 153, 471
Bruzual, G., & Charlot, S. 2003, MNRAS, 344, 1000
Chabrier, G. 2003, PASP, 115, 763
Cibirka, N., Acebron, A., Zitrin, A., et al. 2018, ApJ, 863, 145
Coe, D., Salmon, B., Bradac, M., et al. 2019, ApJ, 884, 85
Dayal, P., & Ferrara, A. 2018, PhR, 780, 1
De Barros, S., Oesch, P. A., Labbé, I., et al. 2019, MNRAS, 489, 2355
Ebeling, H., Qi, J., & Richard, J. 2017, MNRAS, 471, 3305
Egami, E., Kneib, J.-P., Rieke, G. H., et al. 2005, ApJL, 618, L5
Finkelstein, S. L., Ryan, R. E., Jr., Papovich, C., et al. 2015, ApJ, 810, 71
González, V., Labbé, I., Bouwens, R. J., et al. 2011, ApJL, 735, L34
Hashimoto, T., Laporte, N., Mawatari, K., et al. 2018, Natur, 557, 392
Hayes, M., Östlin, G., Schaerer, D., et al. 2010, Natur, 464, 562
Hoag, A., Bradač, M., Brammer, G., et al. 2018, ApJ, 854, 39
Huang, K.-H., Bradač, M., Lemaux, B. C., et al. 2016, ApJ, 817, 11
Ishigaki, M., Kawamata, R., Ouchi, M., et al. 2018, ApJ, 854, 73
Jullo, E., & Kneib, J.-P. 2009, MNRAS, 395, 1319
Labbé, I., Oesch, P. A., Bouwens, R. J., et al. 2013, ApJL, 777, L19
Lee, S.-K., Idzi, R., Ferguson, H. C., et al. 2009, ApJS, 184, 100
Leitherer, C., & Heckman, T. M. 1995, ApJS, 96, 9
Maseda, M. V., Brinchmann, J., Franx, M., et al. 2017, A&A, 608, A4
Meneghetti, M., Natarajan, P., Coe, D., et al. 2017, MNRAS, 472, 3177
Merlin, E., Amorín, R., Castellano, M., et al. 2016, A&A, 590, A30
Merlin, E., Fontana, A., Ferguson, H. C., et al. 2015, A&A, 582, A15
Morishita, T., Trenti, M., Stiavelli, M., et al. 2018, ApJ, 867, 150
Oesch, P. A., van Dokkum, P. G., Illingworth, G. D., et al. 2015, ApJL, 804, L30
Oguri, M. 2010, PASJ, 62, 1017
Oke, J. B. 1974, ApJS, 27, 21
Pacifici, C., Kassin, S. A., Weiner, B. J., et al. 2016, ApJ, 832, 79

Paterno-Mahler, R., Sharon, K., Coe, D., et al. 2018, ApJ, 863, 154
Richard, J., Kneib, J.-P., Ebeling, H., et al. 2011, MNRAS, 414, L31
Ryan, R. E., Jr., Gonzalez, A. H., Lemaux, B. C., et al. 2014, ApJL, 786, L4
Salmon, B., Coe, D., Bradley, L., et al. 2017, arXiv:1710.08930
Salmon, B., Coe, D., Bradley, L., et al. 2018, ApJL, 864, L22
Salmon, B., Papovich, C., Finkelstein, S. L., et al. 2015, ApJ, 799, 183
Schaerer, D., & de Barros, S. 2010, A&A, 515, A73
Senchyna, P., Stark, D. P., Vidal-García, A., et al. 2017, MNRAS, 472, 2608
Smit, R., Bouwens, R. J., Labbé, I., et al. 2014, ApJ, 784, 58
Stark, D. P., Ellis, R. S., Charlot, S., et al. 2017, MNRAS, 464, 469
Whitaker, K. E., Labbé, I., van Dokkum, P. G., et al. 2011, ApJ, 735, 86
Zheng, W., Postman, M., Zitrin, A., et al. 2012, Natur, 489, 406
Zitrin, A., Fabris, A., Merten, J., et al. 2015, ApJ, 801, 44
Zitrin, A., Meneghetti, M., Umetsu, K., et al. 2013, ApJL, 762, L30
Zitrin, A., Seitz, S., Monna, A., et al. 2017, ApJL, 839, L11